

1 **Magma-Hydrothermal Interactions at the Costa Rica Rift from Data Collected in 1994 and**
2 **2015**

3

4 R.P. Lowell¹, L. Zhang³, M.A.M. Maqueda², D. Banyte², V.C.H. Tong³, R.E.R. Johnston⁵, R.N.
5 Harris⁴, R.W. Hobbs⁵, C. Peirce⁵, A.H. Robinson⁵, and K. Kolandaivelu¹

6

7 ¹Department of Geosciences, Virginia Tech, Blacksburg, VA 2406, United States

8 ²School of Natural and Environmental Sciences, Newcastle University, Newcastle, NE1 7RU,
9 United Kingdom

10 ³Department of Earth Sciences, University College London, United Kingdom

11 ⁴College of Ocean and Atmospheric Sciences, Oregon State University, Corvallis, OR 97331,
12 United States (rharris@ceos.oregonstate.edu)

13 ⁵Department of Earth Sciences, Durham University, Lower Mountjoy, South Road, Durham,
14 DH1 3LE, United Kingdom.

15

16

17 **Abstract**

18

19 We use co-located CTD/transmissometry casts and multichannel seismic reflection surveys
20 conducted at the Costa Rica Rift (CRR) to provide a better understanding of magma-
21 hydrothermal processes occurring at an intermediate-rate spreading center. Water column
22 observations reveal an ~200 m thick plume head ~650 m above the seafloor, which corresponds
23 to a hydrothermal heat output of $\sim 200 \pm 100$ MW at the ridge axis. Assuming a hydrothermal
24 vent temperature of 350°C and a discharge area between 10^4 and 10^5 m², this heat output implies
25 a mean crustal permeability within the discharge zone of between 2×10^{-14} and 6×10^{-13} m², and
26 a conductive thermal boundary layer thickness of ~20 m. The volume of magma required to
27 maintain the current hydrothermal heat output over the past two decades should result in an
28 across-axis axial magma lens (AML) width between 270 and 1300 m, depending on the amount
29 of cooling and crystallization. However, seismic reflection images, acquired in 1994 and 2015,
30 while showing an apparent along-axis growth of the AML from 2.4 to 6.0 km between surveys,
31 also suggest that, as of 2015, the AML has an apparent across-axis width of no more than 300 m,
32 and that magma delivery at the intermediate spreading rate CRR may be episodic on time scales
33 of tens of years. The data on magma-hydrothermal interactions at the CRR collected in 1994 and
34 2015 suggest that the hydrothermal system may have significantly cooled and crystallized the
35 AML, primarily in the across-axis direction, and that this hydrothermal system may also
36 episodically turn on and off. The current pattern of microseismicity supports this conclusion,
37 with events not only mirroring the AML depth and location beneath the ridge axis, but also
38 having a temporally varying focus.

39

40 1. Introduction

41

42 An aim of the OSCAR project (*Oceanographic and Seismic Characterization of heat dissipation*
43 *and alteration by hydrothermal fluids at an Axial Ridge*) was to develop a basin-scale model of
44 deep ocean circulation. To this end, a large-scale interdisciplinary geophysical and
45 oceanographic exploration of the Panama Basin, in the eastern Pacific, was conducted between
46 December 2014 and March 2015. A key part of this program focused on the east-west trending,
47 intermediate spreading rate Costa Rica Rift (CRR) (Figure 1), which runs from 3°20'N, 84°11'W
48 to 3°19'N, 83°15'W and is characterized by a 103 km-long rift valley bounded by the Ecuador
49 Fracture Zone to the west and the Panama Fracture Zone to the east. The CRR is asymmetrically
50 spreading with a half rate of 20-25 mm yr⁻¹ to the north (the Cocos Plate) and 35-40 mm yr⁻¹ to
51 the south (the Nazca Plate) [Wilson *et al.*, 2019]. At 3°20'N, 83°44'W, the ridge is divided into
52 two second-order segments by a small non-transform discontinuity (NTD), where the two
53 segment tips overlap by 2.4 km and are offset by ~1.5 km laterally.

54

55 In 1994, RV Maurice Ewing cruise EW9416 imaged a seismic reflector (~2.8 km depth) beneath
56 the bathymetrically shallowest seafloor at the ridge axis (~2900 m below sea level)
57 approximately ~10 km west of the NTD [Buck *et al.*, 1997; Floyd *et al.*, 2002]. In common with
58 seismic reflection studies at other oceanic spreading centers over a range of spreading rates [e.g.,
59 Detrick *et al.*, 1987; Navin *et al.*, 1998; Canales *et al.*, 2006; Singh *et al.*, 2006; Jacobs *et al.*,
60 2007; Van Ark *et al.*, 2007; Carbotte *et al.*, 2013] this reflector was interpreted as evidence of an
61 axial magma lens (AML). As such, this location offered an ideal target to investigate the

62 relationship between crustal heat flow, heat output to the water column, the nature of the heat
63 source and how hydrothermal fluid flow is sustained.

64

65 Consequently, during OSCAR cruise RRS James Cook JC112/113, a number of conductivity,
66 temperature and transmissometry versus depth measurements (henceforth referred to as CTTD
67 data) were made in the water column above the location of the EW9416 seismic line and in the
68 vicinity of the CRR axis [*Banyte et al.*, 2018]. The goal of the CTTD casts was to determine
69 whether there was evidence of current hydrothermal activity in the water column at the ridge
70 axis. Water samples were also collected to determine the ^3He distribution in the water column, in
71 order to characterize and determine the distribution of any hydrothermal emissions.

72

73 In addition, the 1994 multichannel seismic (MCS) survey was also repeated during OSCAR
74 cruise RRS James Cook JC114 [*Hobbs and Peirce*, 2015] to appraise the AML's temporal
75 characteristics and to better constrain its dimensions and extent along-axis. As part of this survey
76 a 3D grid of ocean-bottom seismographs (OBSs) was also deployed across the CRR to provide a
77 ridge-axis velocity model to enable depth conversion [*Zhang et al.*, 2016; 2017]. A vertical array
78 of hydrophones recorded the down-going seismic waveform to enable source signature matching
79 to the 1994 data. MCS lines perpendicular to the ridge axis were also acquired during JC114 to
80 determine the across axis width of the AML (Figure 1); and a transect to the ODP 504B borehole
81 was acquired to provide geophysical versus geological ground truth [*Wilson et al.*, 2019].

82

83 In this paper, we describe the results of co-located water column measurements and seismic
84 reflection images acquired at the CRR, and provide new insights into the coupled magma-

85 hydrothermal interactions at this intermediate spreading ridge system (Figure 2). We apply
86 buoyant plume theory to estimate the heat output of the hydrothermal plume, and use the single
87 pass model [e.g., *Lowell and Germanovich, 2004; Lowell et al., 2013*] to estimate the mass flow
88 rate and crustal permeability at the CRR axis. By combining our heat output estimates with the
89 observed dimensions and extent of the AML in 1994 and 2015, we appraise the role played by
90 the AML in driving hydrothermal circulation. Finally, we speculate on the nature and longevity
91 of hydrothermal fluid flow at the CRR.

92

93 **2. Oceanographic observations of the hydrothermal system**

94

95 Transmissometry data from seven CTTD casts at and near the axis of the CRR (Figure 3a)
96 indicate that there is a measurable decrease in beam transmission over a 200 m-deep zone with
97 its top located ~650 m above the 3150 m-deep seafloor. We interpret this decrease in beam
98 transmission as resulting from a higher concentration of particulate matter within this zone,
99 indicative of a hydrothermal plume reaching neutral buoyancy at this height above seafloor [e.g.,
100 *Baker et al., 1985; Baker and Massoth, 1987*]. Evidence for the presence of hydrothermal
101 activity is also provided by helium isotope data at ocean ridges [e.g., *Lupton, 1998*]. Here the
102 data show an ~50% increase in ^3He concentration at an equivalent depth, compared to
103 background values in the surrounding area (Figure 3b).

104

105 As a hot hydrothermal plume buoyantly ascends from the seafloor it entrains surrounding
106 seawater. As a result of fluid phase separation in the sub-seafloor, the salinity of plume water
107 may be different to that of seawater. The ascending mixture of hydrothermal plume fluid and

108 entrained seawater will gradually reach a level of neutral buoyancy and will then spread laterally
 109 [e.g., *Turner and Campbell*, 1987]. The maximum rise height of the plume is a function of the
 110 buoyancy flux and the density structure of the ocean above, which is described by the Brunt-
 111 Väisälä, or buoyancy, frequency N . The Brunt–Väisälä frequency is defined as $N = \sqrt{-g \rho_z / \rho}$,
 112 where g is the acceleration due to gravity, ρ is potential density, and ρ_z denotes the partial
 113 derivative of ρ with respect to the vertical coordinate, z . We calculate ρ from the CTTD
 114 potential temperature, conductivity/salinity and pressure data using the Thermodynamic
 115 Equation of Seawater -2010 (TEOS-10) formulation [*IOC et al.*, 2010]. From the maximum rise
 116 height of the plume Z^* can be expressed by [*Turner and Campbell*, 1987],

$$118 \quad Z^* = 3.8 F_0^{1/4} N^{-3/4}, \quad (1)$$

119
 120 where the numerical factor 3.8 represents an average rate of entrainment over the height of the
 121 plume as derived from a number of laboratory experiments [*Turner*, 1986]. The buoyancy flux
 122 F_0 is defined as,

$$124 \quad F_0 = Q \frac{\Delta\rho}{\rho_0} g, \quad (2)$$

125
 126 where Q is the volume flow rate in $\text{m}^3 \text{s}^{-1}$ and $\Delta\rho$ is the density difference between hydrothermal
 127 fluid and seawater. Symbols and parameter values are given in Table 1. Although $\Delta\rho/\rho_0$ may
 128 result from both salinity and temperature differences, here we assume that the primary factor is
 129 the difference in temperature. Hence,

130

131 $\Delta\rho/\rho_0 = \alpha\Delta T,$

132

133 where α is the thermal expansion coefficient of seawater. Given that the heat output, H , in the
134 hydrothermal plume is,

135

136 $H = \rho c_p Q \Delta T,$ (3)

137

138 where c_p is the specific heat at constant pressure, the heat output can then be written in terms of
139 the buoyancy flux F_0 or the maximum plume rise height, Z^* , as

140

141 $H = \frac{\rho c_p}{\alpha g} F_0 = \frac{\rho c_p}{\alpha g} \left(\frac{Z^*}{3.8} \right)^4 N^3.$ (4)

142

143 The strong dependence of H on Z^* and N suggests that small errors in these parameters can lead
144 to significant errors in the estimated value of H .

145

146 Figure 3c shows the abyssal density stratification, N^2 , determined from the CTTD casts
147 undertaken at the CRR axis, plotted with depth. The graph shows that N^2 gradually increases
148 with height above seabed, with a sharp change in gradient near 2500 m depth. This depth, which
149 coincides with the top of the zone of decreased transmissivity and interpreted as the top of a
150 hydrothermal plume head (Figure 3a), likely results from a change in ocean dynamics at depths
151 less than 2500 m. The average value of N^2 between 3150 m and 2500 m depth is $\sim 2 \times 10^{-7} \text{ s}^{-2}$.

152

153 Using parameter values from Table 1, a maximum rise height for the plume, and a Z^* of ~ 650 m,
154 we obtain a heat output, H , of $\sim 200 \pm 100$ MW. Uncertainties in H stem from uncertainties in Z^*
155 (± 10 m), N^2 ($\pm 0.5 \times 10^{-7} \text{ s}^{-2}$), and the average value of N^2 at the relevant depth of $0.25 \times 10^{-6} \text{ s}^{-2}$
156 (Figure 3c). This heat output is similar to estimates for hydrothermal systems at other mid-ocean
157 ridges [e.g., *Baker, 2007*], and suggests that the observed CRR plume likely results from a high-
158 temperature black smoker-like system. Data from seafloor hydrothermal systems indicate that
159 although most of the heat output occurs in the form of diffuse flow, 80-90% of hydrothermal
160 heat output is derived from high-temperature magma driven flow [Mittelstaedt et al., 2012;
161 Lowell et al., 2013].

162

163 Although direct measurements of the hydrothermal vent temperature at the CRR are not
164 available, black smoker temperatures are typically $\sim 350^\circ\text{C}$ [e.g., *Lowell et al., 2013*]. Using a ΔT
165 value of 350°C , equation (3) yields a volumetric flow rate of $0.1 \leq Q \leq 0.2 \text{ m}^3 \text{ s}^{-1}$. Assuming that
166 this flow is driven by buoyancy differences between cold recharge fluid and hot vent fluid within
167 the permeable crust, an integrated expression of Darcy's Law (assuming that the main resistance
168 to hydrothermal flow occurs in the discharge zone) enables an estimate of crustal permeability to
169 be made using,

170

$$171 \quad Q = \frac{\alpha_d g k_d T_v A_d}{v_d}, \quad (5)$$

172

173 where k_d is the permeability, T_v is the mean vent temperature, A_d is the area of the discharge
174 zone, and ν_d is the kinematic viscosity. The subscript d is used to indicate properties of the
175 discharge zone.

176

177 Substituting the above values for Q into equation (5) together with the parameter values from
178 Table 1, we obtain $2 \times 10^{-9} \leq k_d A_d \leq 6 \times 10^{-9} \text{ m}^4$. Given that the footprint areas of vent fields are
179 typically observed to lie between 10^4 and 10^5 m^2 [e.g., *Lowell et al.*, 2013], we estimate that the
180 crustal permeability in the CRR hydrothermal discharge region lies between 2×10^{-14} and $6 \times$
181 10^{-13} m^2 , similar to that estimated for many seafloor systems [*Lowell et al.*, 2013].

182

183 Having determined the amount of heat being output into the water column at the CRR, we can
184 now use this estimate to provide an insight into the nature of the heat source, by determining the
185 extent and temporal characteristics of the axial magmatic system as evidenced by the observed
186 AML.

187

188 **3. Seismic observations of the AML**

189

190 To enable direct comparison of the 1994 [along-axis line 1268 (EW9416)] and 2015 [along-axis
191 line NG_Bb13 and across-axis line NG_G10 (JC114)] MCS lines, all lines have been processed
192 in an identical manner to final migrated form [*Zhang et al.*, 2017]. Details of the acquisition can
193 be found in the JC114 cruise report [*Hobbs and Peirce*, 2015] and the processing sequence
194 included: trace editing, divergence correction and amplitude balancing, band-pass filtering,
195 Kirchhoff pre-stack time migration, muting, stacking, and noise suppression. To maintain

196 consistency in data processing between surveys, the pre-stack time migration of both along-axis
197 lines was applied with the same velocity model, which was based on the velocity analysis of line
198 1268, and waveform matching between the 1994 and 2015 surveys was applied based on the
199 vertical hydrophone recording of the down-going waveform during JC114. MCS image depth
200 conversion was undertaken using a sub-seabed velocity structure and was derived from modeling of
201 OBS and MCS gather travel-time picks [*Wilson et al.*, 2019; *Robinson et al.*, in revision].

202
203 Both MCS surveys image an AML at approximately the same two-way travel time (TWTT) sub-
204 seabed (Figure 4). The reprocessed line 1268 from the original 1994 survey (Figure 4a), shows a
205 2.4 km-long reflection event at 5.1 to 5.3 s two-way travel time (TWTT). The 2.38 km s^{-1}
206 stacking velocity of this event precludes it from being a water-path scattered event or a sea
207 surface/water bottom multiple. Modeling of the near-offset traces in the unstacked gathers
208 (Figure 5) shows that the reflection event corresponds to a thin, low velocity anomaly, where the
209 velocity may be as low as 4.5 km s^{-1} , and where its thickness may be of the order of $\sim 100 \text{ m}$.
210 Using the background upper crustal velocity model, the AML imaged in 1994 has an apparent
211 eastward dip, lying between 3.0-3.5 km below the seafloor.

212
213 Line NG_Bb13, from the more recent 2015 resurvey, was navigated to the location of line 1268
214 to better than the Fresnel radius of $\sim 500 \text{ m}$ at AML depth, assuming a dominant frequency of 20
215 Hz. This line (Figure 4b) also images the AML reflection at 5.1 to 5.3 s TWTT (3.0-3.5 km
216 below the seafloor), suggesting a consistency of melt supply to the ridge-axis with at least an
217 ~ 20 -year episodicity, that also arrives at 5.1 to 5.3 s TWTT (3.0-3.5 km below the seafloor). This
218 reflection event has a total length of $\sim 6 \text{ km}$, where the additional length results from an extension

219 westward from the AML as originally imaged in 1994. Along-axis variation in reflection true
220 amplitude suggests that, as of 2015, the AML may possibly be split into two limbs, with a gap of
221 ~600 m between them (Figure 4b). The eastern limb effectively mirrors that of line 1268, but
222 extends westward for ~650 m, whereas the western limb, which is only observed on line
223 NG_Bb13, extends the AML an additional 2.5 km.

224

225 AMLs detected along the intermediate spreading Juan de Fuca Ridge [*Van Ark et al., 2007*] and
226 the fast spreading East Pacific Rise [*Carbotte et al., 2013*], typically have an across-axis width of
227 between ~500 and 1000 m. However, the orthogonal line NG_G10 (Figure 4c) from the 2015
228 survey does not show a similar expression of an AML reflection event. This observation at the
229 CRR may indicate that the width of the AML is similar to the lateral resolution of the seismic
230 signal which, for the 20 Hz peak frequency, suggests a width of no more than ~60 m. The line
231 NG_G10 image possibly shows a narrow-width event whose diffraction would intersect line
232 NG_Bb13 at the time of the imaged AML reflection. The event is no more than 300 m wide,
233 which we assume as an estimate for the maximum-width case analyzed below. The apparently
234 narrow width of the AML at the CRR could possibly indicate enhanced lateral hydrothermal
235 circulation that rapidly freezes the melt lens in both off-axis directions. Based on the above we
236 estimate the areal extent of the AML, as of 2015, to be less than $\sim 1.8 \times 10^6 \text{ m}^2$.

237

238 **4. Link between AML and hydrothermal heat output**

239

240 Using the estimated heat output at the CRR of ~200 MW and an estimated magma heat transfer
241 area (A_m) of $1.8 \times 10^6 \text{ m}^2$, we construct a simple heat balance model for heat transfer from the

242 AML to the hydrothermal system. We assume conduction across a thermal boundary layer of
243 thickness, δ , following *Lowell and Germanovich* [2004] and *Lowell et al.* [2013],

244

$$245 \quad H = \frac{\lambda(T_m - T_v / 2)A_m}{\delta}, \quad (6)$$

246

247 where λ is the thermal conductivity of the host rock, and T_m is the mean temperature of the
248 AML. Using parameters defined in Table 1, and the subscript m to indicate properties of the
249 magma, we obtain a thermal boundary layer of thickness of ~ 20 m, similar to estimates for other
250 ridge axis systems [*Lowell et al.*, 2013] and ophiolites and tectonic windows [e.g., *Gillis*, 2008].

251 Our estimated uncertainty in δ is ± 10 m primarily based on the uncertainty in H and we note that
252 the thermal boundary layer thickness scales linearly with A_m , so a smaller A_m would yield a
253 smaller δ .

254

255 However, to maintain the estimated heat output in a quasi-steady-state, this thermal boundary
256 layer must retain an effectively constant thickness [*Lowell and Germanovich*, 2004] which, in
257 turn, necessitates the influx of fresh magma into the AML [*Liu and Lowell*, 2009; *Choi and*
258 *Lowell*, 2015]. Following *Lowell et al.* [2013] we assume that the observed hydrothermal heat
259 output is driven by heat transfer from the magma that has replenished the AML, cooled and
260 partially crystalized between 1994 and 2015. The mean rate of magma replenishment, dV_m/dt ,
261 needed to maintain a hydrothermal heat output can be written as,

262

$$263 \quad H = (\rho_m c_m \Delta T + \rho_m \chi L)(dV_m / dt), \quad (7)$$

264

265 where χ is the crystal fraction, and the first term in parenthesis on the right side of equation (7) is
266 the sum of the sensible and latent heat released as the melt cools and crystallizes. Although the
267 MCS data do not provide direct information regarding the state of the AML volume, internal
268 temperature and crystal content, the images do show that the AML still exists where it was first
269 imaged in 1994, and further show that it has apparently doubled in length, largely westwards.
270 Hence the MCS data suggest magma replenishment and AML growth between 1994 and 2015,
271 either constantly or episodically, since in this time frame the AML imaged in 1994 would
272 otherwise have solidified, and hydrothermal heat output that may have been present in 1994
273 would have declined. Without magma replenishment, crystal suspended simulations of AML
274 cooling show a rapid decrease in heat output and hydrothermal temperature such that
275 crystallinity reaches 60% in less than 10 years [*Liu and Lowell, 2009*].

276

277 Although mid-ocean ridge magma supply shows variability on decadal time scales, we start by
278 estimating the mean rate of magma replenishment required to maintain the hydrothermal system
279 at a quasi-steady-state heat output of 200 MW for the past two decades. We assume quasi-
280 steady-state input magma at its liquidus temperature. For simplicity, we further assume that each
281 initial cooling of 10°C leads to 5% fractional crystallization [*MacLennan, 2008; Lowell et al.,*
282 *2013*]. If magmatic heat transfer is accompanied by cooling of 20°C, as observed at 9°50'N at the
283 East Pacific Rise between the eruptions of 1991/1992 and 2005/2006 [*Goss et al., 2010*], the heat
284 released by cooling of the replenished magma is $\sim 60 \text{ MJ m}^{-3} + \sim 110 \text{ MJ m}^{-3}$, corresponding to
285 the sensible and latent heat respectively, or $\sim 170 \text{ MJ m}^{-3}$ in total. Substituting this value of heat
286 release into equation (7) yields a magma replenishment rate, dV_m/dt , of $\sim 1.2 \text{ m}^3 \text{ s}^{-1}$. With these

287 assumptions and values the amount of magma replenishment between 1994 and 2015 would be
288 $\sim 7.8 \times 10^8 \text{ m}^3$. Given that the maximum vertical cross-sectional area of the AML is $\sim 6 \times 10^3 \text{ m}$ -
289 long x 100 m-deep, the amount of magma needed to sustain the hydrothermal system would
290 extend $\sim 1300 \text{ m}$ across-axis, more than four times the upper estimate of $\sim 300 \text{ m}$ suggested by the
291 2015 MCS data images, and well within the navigational precision of both the 1994 and 2015
292 surveys. If cooling and/or crystallization is greater as might be expected from hydrothermal
293 circulation a smaller magma replenishment rate is possible. For example, if the amount of
294 magma cooling is 100°C , with 50% crystallization, the resulting rate of magma replenishment
295 needed to sustain the 200 MW hydrothermal system would be $0.24 \text{ m}^3 \text{ s}^{-1}$ and the volume of
296 magma emplaced would be $1.6 \times 10^8 \text{ m}^3$. In this scenario the expected across-axis width of the
297 AML would be $\sim 270 \text{ m}$, which is of the same order as the putative AML width.

298

299 It is also possible, however, that magma replenishment is episodic even on a 20-year time scale
300 and that hydrothermal heat output would then wax and wane in that time frame. Finite width
301 dikes in layer 2B suggest discrete intrusion events every 10-100 years [*Head et al.*, 1996]. At an
302 intermediate spreading center such as the CRR magma replenishment is likely to be more
303 infrequent than at the fast spreading East Pacific Rise over long time scales. If the plume
304 represented the heat from a single replenishment event, the volume of magma needed to generate
305 the 200 MW of heat would scale with time since the event.

306

307 **5. Discussion**

308

309 CTTD data indicates the presence of a hydrothermal plume above the CRR, that has a heat
310 output of $\sim 200 \pm 100$ MW. MCS images have enabled estimation of AML dimensions and
311 magma replenishment characteristics at the CRR. Our modeling results assume quasi-steady state
312 behavior. However, the MCS data may, instead, be suggesting episodic AML replenishment. The
313 contrasting pattern of AML reflectivity between the 1994 and 2015 surveys (Figure 4) suggests
314 that the western region of the ridge axis is the current focus of magma replenishment, and that it
315 could possibly be disconnected from the eastern limb as a result of rapid, focused, hydrothermal
316 cooling. Alternatively, the two limbs may be joined, supplied via a single magma source, with
317 the apparent gap between the western and eastern limbs an artifact of out-of-plane interference
318 and scattering of seismic energy by the rugged seafloor topography above. The lack of a clear
319 across-axis reflection event from the AML suggests a narrow width perpendicular to the
320 spreading direction, whereby the AML appears to be a ribbon of magma extending ~ 6 km along
321 the ridge axis with a maximum width of 300 m, significantly narrower than AMLs observed at
322 other intermediate [e.g., *Van Ark et al.*, 2007] or the faster spreading ridges [e.g., *Kent et al.*,
323 1993].

324

325 The extent of the AML along axis suggests significant westward magma replenishment has
326 occurred, raising the question of whether the inferred volume of magma replenishment required
327 to maintain a 200 MW hydrothermal system can do so for two decades, or instead if the
328 replenishment process is more likely to be episodic. Assuming that magma is added to the AML
329 over its entire current length of ~ 6 km, we find that to maintain a 200 MW hydrothermal system
330 for 20 years, the across-axis width of the AML would have to range between ~ 270 and 1300 m,
331 depending on the degree of cooling and crystallization assumed. Given the estimated AML

332 width, it is possible that either the observed hydrothermal heat output is a result of
333 significant/enhanced cooling of a consistent magma replenishment, or a result of more recent
334 replenishment focused towards the western end of the ridge axis. Numerical models of two-phase
335 flow in NaCl-H₂O systems indicate that there is a lag time of years to decades between the decay
336 of heat input at the base of the system and changes in seafloor vent temperatures and heat output
337 [Singh *et al.*, 2013; Choi and Lowell, 2015]. Consequently, the currently observed heat output
338 may reflect an episode of magma replenishment in the recent past (years to decades), and the
339 westward extending AML reflectivity suggests, in turn, an apparently thin ribbon of recent
340 magma replenishment into the AML that has yet to spread in the across axis direction.

341

342 A new episode of magma input, associated with a phase of diking, may generate an event plume
343 [e.g., Baker *et al.*, 1987, 1998; Lowell and Germanovich, 1995]. In this case, the heat output and
344 ³He anomaly recorded in the observed water column plume may reflect a transient event rather
345 than be an indication of quasi-steady-state hydrothermal heat flux. A repeat CTTD survey
346 conducted two weeks later in the same area (Figure 3b) failed to detect the plume which may
347 support a transitory cause or, more simply, a change in ocean currents or tidal flows may have
348 displaced it from its previously observed location.

349

350 One hundred and sixteen of the more significant microearthquakes recorded during the 2015
351 OBS survey were hand-picked, and their hypocenters projected onto a depth-converted migrated
352 image of line NG_Bb13 (Figure 6). These locations were estimated using the NonLinLoc
353 software (Lomax *et al.*, 2000) based on a 1D crustal velocity model derived from modeling of
354 both OBS and MCS gather travel time picks [Wilson *et al.*, 2019; Robinson *et al.*, in revision].

355 This analysis shows that the majority of these events recorded during a 21-day period are
356 distributed at or above the AML between 83°48'W and 83°52'W. Analyzing the distribution of
357 seismicity suggests that there are two principal event populations. The initial cluster of
358 seismicity, between Julian days (JD) 26-34, is located above and to the east of the gap between
359 the two AML limbs, and extends from AML depth to the seabed. It is not clear whether there is a
360 discernible migration in the depth of seismicity, either upward or downward, over the period of
361 this cluster. However, similar observations elsewhere [e.g., *Tolstoy et al.* 2008; *Dziak et al.*,
362 2007] correlate such seismicity with the existence of active, high-temperature hydrothermal
363 circulation within the upper crust that would transfer heat from the underlying AML. This
364 correlation between heat source and seismicity may, therefore, reflect hydraulic fracturing within
365 the hydrothermal circulation system [e.g., *Wilcock et al.*, 2009]. Further, *Fontaine et al.* [2011]
366 predict that localized hydrothermal cells will cause along strike variation in the size of an AML
367 on a scale-length of hundreds of meters, so our estimate of the AML width under the CRR, based
368 on a single MCS line, even though repeated, is open to debate. Possible evidence for this
369 interaction is provided by the second cluster, between JD 35-47, which predominantly occurs
370 above the western AML limb and is confined to depths >5 km, suggesting that this population
371 may be related to changes in the AML volume. The apparent lack of seismicity between the
372 AML and the NTD may also suggest the presence of a cooling front, limiting eastward melt
373 migration.

374

375 Although our analysis of magma-hydrothermal interactions at the CRR suggests that magma
376 supply may be episodic even on a decadal scale, episodic magma supply likely occurs over much
377 longer time scales as well. Hence the ridge axis may, therefore, evolve through alternating

378 phases of tectonism and magmatic accretion [*Kappel and Ryan, 1986*]. This interpretation is
379 supported by off-axis observations at the CRR [*Wilson et al., 2019*] which demonstrate the
380 variable crustal formation modes that have occurred at this ridge system over 7 Ma. We suggest,
381 therefore, that intermediate spreading ridge systems may represent a finely balanced
382 environment, where changes in the rates of magma supply, tectonic extension, and hydrothermal
383 cooling may shift the equilibrium state towards different end-member spreading modes.

384

385 **6. Conclusions**

386

387 The combination of water column data and repeat multichannel seismic surveys at the CRR axis
388 enables us to make a preliminary appraisal of magma-hydrothermal interactions at this
389 intermediate spreading ridge. The results suggest that current hydrothermal heat output at the
390 CRR may be the result of continuous or episodic magma replenishment, that has undergone
391 significant cooling by hydrothermal circulation. Alternatively, the observed hydrothermal plume
392 may represent a transient event such as an event plume associated with a recent input of magma
393 into the AML coupled with a phase of diking. In either case, the MCS data clearly show both
394 temporal and spatial changes in AML characteristics at the CRR axis on a decadal time scale,
395 and these changes may be reflected in corresponding changes in hydrothermal discharge.
396 Additional information on the state of the CRR hydrothermal system is required to determine
397 whether it is in a decaying or a growing phase, which can only be gleaned from a detailed
398 seafloor morphological and sampling study, supported by a high-resolution 3D volume seismic
399 survey to correctly map the location of the AML both along and across the ridge axis.

400

401 **Acknowledgements**

402 This research project was funded by the National Science Foundation grants OCE 1353114 and
403 1558797 to RPL, NSF grants OCE 1353003 and 1558824 to RNH, and by the Natural
404 Environmental Research Council (NERC) grants NE/I027010/1 to Durham University (RWH
405 and CP), NE/I022868/1 and NE/I022868/2 to the University of Newcastle (MAAM), and
406 (NE/I022957) to University College, London (VCHT). We would like to thank all those
407 involved in the planning and acquisition of data during research cruises JC112/3 and JC114,
408 including the officers, engineers and crew of the RRS James Cook, the scientific party, and all
409 seagoing NERC facility technicians and engineers. The MCS data were processed using GLOBE
410 Claritas[™], and manipulated for plotting using Seismic Unix. The MCS source characteristics
411 were recorded by the NERC Ocean-Bottom Instrumentation Facility (*Minshull et al.*, 2005).
412 Figures were prepared using the Generic Mapping Tools (GMT). Data from JC112/3 and JC114
413 are archived at the NERC's British Oceanographic Data Center and at Durham University, and
414 are available on request. Two anonymous reviewers helped us improve the clarity of this paper.
415 Sadly, Bob Lowell passed away while this, his last paper, was in review. Throughout his long
416 career, Bob made major contributions to our understanding of the thermal and fluid dynamics of
417 hydrothermal systems and the characteristics of their magma-source drivers. In this OSCAR
418 project, we greatly benefited from that wealth of knowledge and, in particular, his geological
419 insights into the interpretation of the geophysical and oceanographic imaging. The final
420 accepted version of this manuscript is available through Durham Research Online
421 (dro.dur.ac.uk).

422

423 **References**

424

425 Baker, E.T. (2007), Hydrothermal cooling of Mid-Ocean Ridge axes: Do measured and modeled
426 heat fluxes agree?, *Earth Planet. Sci. Lett.*, 263, 140-150, doi:10.1016/j.epsl.2007.09.010.

427

428 Baker, E.T. and G.J. Massoth (1987), Characteristics of hydrothermal plumes from two vent
429 fields on the Juan de Fuca Ridge, northeast Pacific Ocean, *Earth Planet. Sci. Lett.*, 85, 59-
430 73, doi:10.1016/0012-821X(87)90021-5.

431

432 Baker, E.T., J.W. Lavelle and G.J. Massoth (1985), Hydrothermal particle plumes over the
433 southern Juan de Fuca Ridge, *Nature*, 316, 342-344.

434

435 Baker, E.T., G.J. Massoth and R.A. Feely (1987), Cataclysmic hydrothermal venting on the Juan
436 de Fuca Ridge, *Nature*, 329, 149-151.

437

438 Baker, E.T., G.J. Massoth, R.A. Feely, G.A. Cannon and R.E. Thomson (1998), The rise and fall
439 of the CoAxial hydrothermal site, 1993-1996, *J. Geophys. Res.*, 103, 9791-9806,
440 doi:10.1029/97JB03112.

441

442 Banyte D, M.A. Morales Maqueda, D.A. Smeed, R. Hobbs, A. Megann, and S. Recalde (2018),
443 Geothermal heating in the Panama Basin: 1. Hydrography of the Basin. *J. Geophys. Res.*
444 *Oceans*, 123, 7382-7392, doi:10.1029/2018JC13868.

445

446 Buck, W.R., S.M. Carbotte and C. Mutter (1997), Controls on extrusion at mid-ocean ridges,
447 *Geology*, 25, 935-938, doi:10.1130/0091-7613(1997)025<0935:COEAMO>2.3.CO;2.
448

449 Canales, J.P., S.C. Singh, R.S. Detrick, S.M. Carbotte, A. Harding, G.M. Kent, J.B. Diebold, J.
450 Babcock and M.R. Nedimovic (2006), Seismic evidence for variations in axial magma
451 chamber properties along the southern Juan de Fuca Ridge, *Earth Planet. Sci. Lett.*, 246,
452 353-366, doi:10.1016/j.epsl.2006.04.032.
453

454 Carbotte, S.M., M. Marjanovic, H. Carton, J.C. Mutter, J.P. Canales, M.R. Nedimovic, S. Han
455 and M.R. Perfit (2013), Fine-scale segmentation of the crustal magma reservoir beneath the
456 East Pacific Rise, *Nature Geosci.*, doi:10.1038/NGEO1933.
457

458 Choi, J. and R.P. Lowell (2015), The response of two-phase hydrothermal systems to changing
459 magmatic heat input at mid-ocean ridges, *Deep Sea Res II*, 121, 17-30,
460 doi:10.1016/j.dsr2.2015.05.005.
461

462 Detrick, R.S., P. Buhl, E. Vera, J. Mutter, J. Orcutt, J. Madsen and T. Brocher (1987), Multi-
463 channel seismic imaging of a crustal magma chamber along the East Pacific Rise, *Nature*,
464 326, 35-41.
465

466 Dziak, R.P., D.R. Bohnenstiehl, J.P. Cowen, E.T. Baker, K.H. Rubin, J.H. Haxel and M.J.
467 Fowler (2007), Rapid dike emplacement leads to eruptions and hydrothermal plume release
468 during seafloor spreading events, *Geology*, 35, 579-582, doi:10.1130/G23476A.1.

469

470 Floyd, J.S., J.C. Mutter and S.M. Carbotte. (2002), Seismic reflection imaging of the evolution of
471 ocean crustal structure at the intermediate rate spreading Costa Rica Rift, *EOS Trans. AGU*,
472 83, Fall Meeting Suppl., Abstract T12-1318.

473

474 Fontaine, F.J., J.-A. Olive, M. Cannat, J. Escartin and T. Perol (2011), Hydrothermally-induced
475 melt lens cooling and segmentation along the axis of fast-and intermediate-spreading
476 centers, *Geophys. Res. Lett.*, 38, L14307, doi:10.1029/2011GL047798.

477

478 Gillis, K.M., (2008), The roof of an axial magma chamber: A hornfelsic heat exchanger,
479 *Geology*, 36, 292-302, doi:10.1130/G24590A.1.

480

481 GLOBE Claritas Software Documentation 6.0.1 (2012), Institute of Geological and Nuclear
482 Sciences, Ltd.

483

484 Goss, A.R., M.R. Perfit, W.I. Ridley, K.H. Rubin, G.D. Kamenow, S.A. Soule, A. Fundis and
485 D.J. Fornari (2010), Geochemistry of lavas from the 2005-2006 eruption at the
486 East Pacific Rise, 9°46'-9°56'N: Implications for ridge crest plumbing and decadal changes
487 in magma chamber composition, *Geochem. Geophys. Geosyst.*, 11, Q05T09
488 doi:10.1029/2009GC02977.

489

490 Head, J. W.III, L. Wilson and D.K. Smith (1996), Mid-ocean ridge eruptive vent morphology
491 and substructure, *J. Geophys. Res.*, 101, 28,265–28,280, doi:10.1029/96JB02275.

492
493 Hobbs, R.W. and C. Peirce (2015), RRS James Cook JC114 cruise report, 74pp.
494
495 IOC, SCOR and IAPSO (2010), The international thermodynamic equation of seawater –
496 2010: Calculation and use of thermodynamic properties, Intergovernmental
497 Oceanographic Commission, Manuals and Guides No. 56, UNESCO (English), 196 pp.
498
499 Jacobs, A.M., A.J. Harding and G.M. Kent (2007), Axial structure of the Lau back-arc basin
500 from velocity modeling of multichannel seismic data, *Earth Planet. Sci. Lett.*, 259, 239-255,
501 doi:10.1016/j.epsl.2007.04.021.
502
503 Kappel, E.S. and W.B.F Ryan (1986), Volcanic episodicity and a non-steady-state rift valley
504 along northeast Pacific spreading centers: Evidence from SeaMARC I, *J. Geophys. Res.*,
505 91(3), 13925–13940, doi:10.1029/JB091iB14p13925.
506
507 Kent, G.M., A.J. Harding and J.A. Orcutt (1993), Distribution of magma beneath the East Pacific
508 Rise between the Clipperton Transform and the 9°17' N deval from forward modelling of
509 common depth point data, *J. Geophys. Res.*, 98, 13,945-13,969, doi:10.1029/93JB00705.
510
511 Liu, L. and R.P. Lowell (2009), Models of hydrothermal heat output from a convecting,
512 crystallizing, replenished magma chamber beneath an oceanic spreading center, *J. Geophys.*
513 *Res.*, 114, B02102, doi:10.1029/2008JB005846.
514

515 Lomax, A., J. Virieux, P. Volant and C. Berge-Thierry (2000), Probabilistic earthquake location
516 in 3D and layered models: Introduction of a Metropolis-Gibbs method and comparison with
517 linear locations, In: *Advances in seismic event location*, edited by C.H. Thurber and N.
518 Rabinowitz, Kluwer, Dordrecht, 101-134, doi:10.1007/978-94-015-9536-0_5.

519

520 Lowell, R.P. and L.N. Germanovich (1995), Dike injection and the formation of megaplumes
521 at ocean ridges, *Science*, 267, 1804-1807, doi:10.1126/science.267.5205.1804.

522

523 Lowell, R.P. and L.N. Germanovich (2004), Seafloor hydrothermal processes: Results from scale
524 analysis and single-pass models, in *Mid-Ocean Ridges: Hydrothermal Interactions Between*
525 *the Lithosphere and Oceans*, *Geophys. Monogr. Ser.*, vol. 148, ed. by C.R. German, J. Lin,
526 and L.M. Parson, pp. 219-244, AGU, Washington, D.C.

527

528 Lowell, R.P., A. Farough, J. Hoover and K.C. Cummings (2013), Characteristics of magma-
529 driven hydrothermal systems at oceanic spreading centers, *Geochem. Geophys. Geosyst.*, 14,
530 1756-1770, doi:10.1002/ggge.20109.

531

532 Lupton, J. (1998), Hydrothermal helium plumes in the Pacific Ocean, *J. Geophys. Res.*, 103,
533 15,853–15,868, doi:10.1029/98JC00146.

534

535 Maclennan, J. (2008), The supply of heat to mid-ocean ridges by crystallization and cooling of
536 mantle melts, in *Magma to Microbe: Modeling Hydrothermal Processes at Ocean Spreading*
537 *Centers*, *Geophys. Monogr. Ser.*, vol. 178, edited by R. P. Lowell, J. S. Seewald, A.

538 Metaxas, and M.R. Perfit, 285 pp., AGU, Washington D. C., doi:10.1029/GM178.
539
540 Mittelstaedt, E., J. Escartin, N. Gracias, J.-A. Olive, T. Barreyre, A. Davaille, M. Cannat, R.
541 Garcia (2012), Quantifying diffuse and discrete venting at the Tour Eiffel vent site, Lucky
542 Strike hydrothermal field, *Geochem. Geophys. Geosys.*, 13, Q04008,
543 doi:10.1029/2011GC003991.
544
545 Minshull, T.A., M.C. Sinha and C. Peirce (2005). Multi-disciplinary, sub-seabed geophysical
546 imaging: a new pool of 28 seafloor instruments in use by the United Kingdom Ocean
547 Bottom Instrument Consortium. *Sea Technology*, 46(10), 27-31.
548
549 Navin, D.A., C. Peirce and M.C. Sinha, (1998), The RAMESSES experiment - II - Evidence for
550 accumulated melt beneath a slow-spreading ridge from wide-angle refraction and
551 multichannel reflection profiles. *Geophys. J. Int.*, 135 (3), 746-772, doi:10.1046/j.1365-
552 246X.1998.00709.x.
553
554 Singh, S.C., W.C. Crawford, H. Carton, T. Seher, V. Combier, M. Cannat, J.P. Canales, D.
555 Dusunur, J. Escartín and J.M. Miranda (2006), Discovery of a magma chamber and faults
556 beneath a Mid-Atlantic Ridge hydrothermal field, *Nature*, 442, 1029–1032,
557 doi:10.1038/nature05105.
558

559 Singh, S., R.P. Lowell and K.C. Lewis (2013), Numerical modeling of phase separation at the
560 Main Endeavour Field, Juan de Fuca Ridge, *Geochem. Geophys. Geosyst.*, *14*, 4021-4034,
561 doi:10.1002/ggge.20249.

562

563 Stockwell, J.W. (1999), The CWP/SU: Seismic un*x package, *Computers and Geosciences*, *25*,
564 415-419, doi:10.1016/S0098-3004(98)00145-9.

565

566 Tolstoy, M., F. Waldhauser, D.R. Bohnenstiehl, R.T. Weekly and W.-Y. Kim (2008), Seismic
567 identification of along-axis hydrothermal flow on the East Pacific Rise, *Nature*, *451*,
568 doi:10.1038/nature06424.

569

570 Turner, J.S. (1986), Turbulent entrainment: the development of the entrainment assumption
571 and its application to geophysical flows, *J. Fluid Mech.*, *173*, 431-471,
572 doi:10.1017/S0022112086001222.

573

574 Turner, J.S. and I.H. Campbell (1987), Temperature, density and buoyancy flux in “black
575 smoker” plumes, and the criterion for buoyancy reversal, *Earth Planet. Sci. Lett.*, *86*, 85-92,
576 doi:0.1016/0012-821X(87)90191-9.

577

578 Van Ark, E.M., R.S. Detrick, J.P. Canales, S.M. Carbotte, A.J. Harding, G.M. Kent, M.R.
579 Nedimović, W.S.D. Wilcock, J.B. Diebold and J.M Babcock (2007), Seismic structure of the
580 Endeavour Segment, Juan de Fuca Ridge: Correlations with seismicity and hydrothermal
581 activity, *J. Geophys. Res.*, *112*, B02401, doi:10.1029/2005JB004210.

582
583
584
585
586
587
588
589
590
591
592
593
594
595
596
597
598
599
600

Wilcock, S.D., E.E. Hoofst, D.R. Toomey, P.R. McGill, A.H. Barclay, D.S. Stakes, and T.M. Ramirez (2009), The role of magma injection in localizing black-smoker activity, *Nat. Geosci.*, 2, 509-513, doi:10.1038/NGEO0550.

Wilson, D.J., A.H. Robinson, R.W. Hobbs, C. Peirce, and M.J. Funnell (2019), Does intermediate spreading-rate oceanic crust result from episodic transition between magmatic and magma-dominated, faulting-enhanced spreading? — The Costa Rica Rift example, *Geophys. J. Int.*, 218, 1617–1641, <https://doi.org/10.1093/gji/ggz184>.

Zhang L., V.C.H. Tong, R.W. Hobbs and D.J. Wilson (2016), 3D crustal structure beneath the Costa Rica Rift from seismic tomography: Insight into magmatic activity, *AGU*, Fall Meeting Abstract T22C-02.

Zhang, L., V.C.H. Tong, R.W. Hobbs, C. Peirce, R. Lowell, G. Haughton, B.J. Murton, M.A. Morales Maqueda and A. Robinson (2017), Axial crustal structure of the Costa Rica Rift: Implications for along-axis hydrothermal circulation, *AGU*, Fall Meeting Abstract T31C-06.

601 **Figure Captions**

602

603 Figure 1. Swath bathymetry map of the Costa Rica Rift (CRR). Black dashed lines mark the
604 cruise track of JC114 in the vicinity of the CRR axis. Solid black lines show the locations of
605 MCS profiles NG_Bb13, 1268 and NG_G10; red triangles indicate OBS locations; blue and red
606 crosses indicate CTTD cast locations discussed in this study. Inset (top right) shows location of
607 the study area (blue rectangle) in the Panama Basin. Principal bathymetric and tectonic features
608 are labelled: the Cocos Ridge, the Galapagos Islands, the Carnegie Ridge, the Malpelo Ridge, the
609 Ecuador Trench, the Galapagos Spreading Ridge (GSR), the Inca Transform (IT), the Ecuador
610 Rift (ER), the Ecuador Fracture Zone (EFZ), the Costa Rica Rift (CRR), and the Panama
611 Fracture Zone (PFZ). The relative plate motion between the Cocos and Nazca plates is shown
612 (mm/yr) along with the location of the ODP site 504B.

613

614 **Figure 2.** Schematic of heat balance model linking axial magma lens heat content to plume heat
615 content showing the relationship of some of the important parameters.

616

617 **Figure 3.** (a) CTD/transmissometry (CTTD) casts along Costa Rica Rift axis showing decreased
618 transmissivity between 2500 m to 2800 m depth. Ridge axis is 3150 m depth. Red curve is a
619 mean of seven profiles (black curves); (b) Results from $\Delta^3\text{He}$ analyses from water samples taken
620 over the CRR at CTTD 6 (09-12-2014, blue points) and CTTD 55 (02-01-2015, red points). Note
621 the elevated value within the depth range of decreased transmissivity. (c) Abyssal stratification
622 over the ridge axis, where N^2 is a squared Brunt-Väisälä frequency. Black lines show individual
623 casts. Dotted and solid red lines show averages displaying higher and lower order data trends

624 respectively. Solid horizontal gray line indicates the top of the transmissivity and $\Delta^3\text{He}$
625 anomalies, and change in slope of N^2 , interpreted as representing the top of the plume. Dashed
626 horizontal gray line indicates the base of the transmissivity anomaly.

627

628 **Figure 4.** Seismic reflection images of the axial magma lens (AML) for MCS profiles shown on
629 Figure 1. (a) Line 1268 from the 1994 survey. (b) Line NG_Bb13 and (c) line NG_G10 from the
630 2015 survey. Black dots indicate the AML reflection at $\sim 5.1\text{-}5.3$ s TWTT. Comparing the
631 stacked image of the AML in (a) with that in (b), we can observe that AML extends westward
632 and its length increases from 2.4 to 6.0 km during the 21 years that separate the surveys.
633 Locations of the non-transform discontinuity (NTD), the intersections between N-S and E-W
634 lines and the average spreading rates over the past 4 My [*Wilson et al.*, 2019] between the Cocos
635 and Nazca plates are labelled.

636

637 **Figure 5.** 1-D five-layer velocity-depth model (a) and its corresponding reflectivity (b) used to
638 forward modelling a CDP gather [after *Wilson et al.*, 2019]. The black line denotes P-wave
639 velocity (V_p), the red line S-wave velocity (V_s) and the green line density (ρ). The solid and
640 dashed blue lines show the OBS and MCS inversion derived 1-D velocity structure at the ridge
641 axis respectively, and the dotted purple line shows the OBS forward modelling 1-D velocity
642 structure (all from *Wilson et al.*, 2019). (c) Synthesized waveforms and (d) observed records of
643 an example CDP gather (1217 from line 1268) with trace offsets incrementing every 25 m and
644 ranging from 187.5 m to 462.5 m. The seabed (water-bottom) and AML reflections are labeled.

645

646 **Figure 6.** Microseismicity at the CRR. (a) Swath bathymetry of the CRR. Inverted red triangles
647 indicate OBS locations used for picking and relocating earthquake locations. Dots are earthquake
648 hypocenters, colored by elapsed time in Julian days since the start of 2015. Black line shows the
649 location of line NG_Bb13. (b) Depth distributions of hypocenters across the ridge axis. (c) Depth
650 distributions of hypocenters along the ridge axis overlaid on a time-to-depth converted migrated
651 seismic image of line NG_Bb13. The majority of microearthquakes are located directly above
652 the AML. The location of the NTD is labelled.

653

654

655 **Table 1. Symbols and parameters**

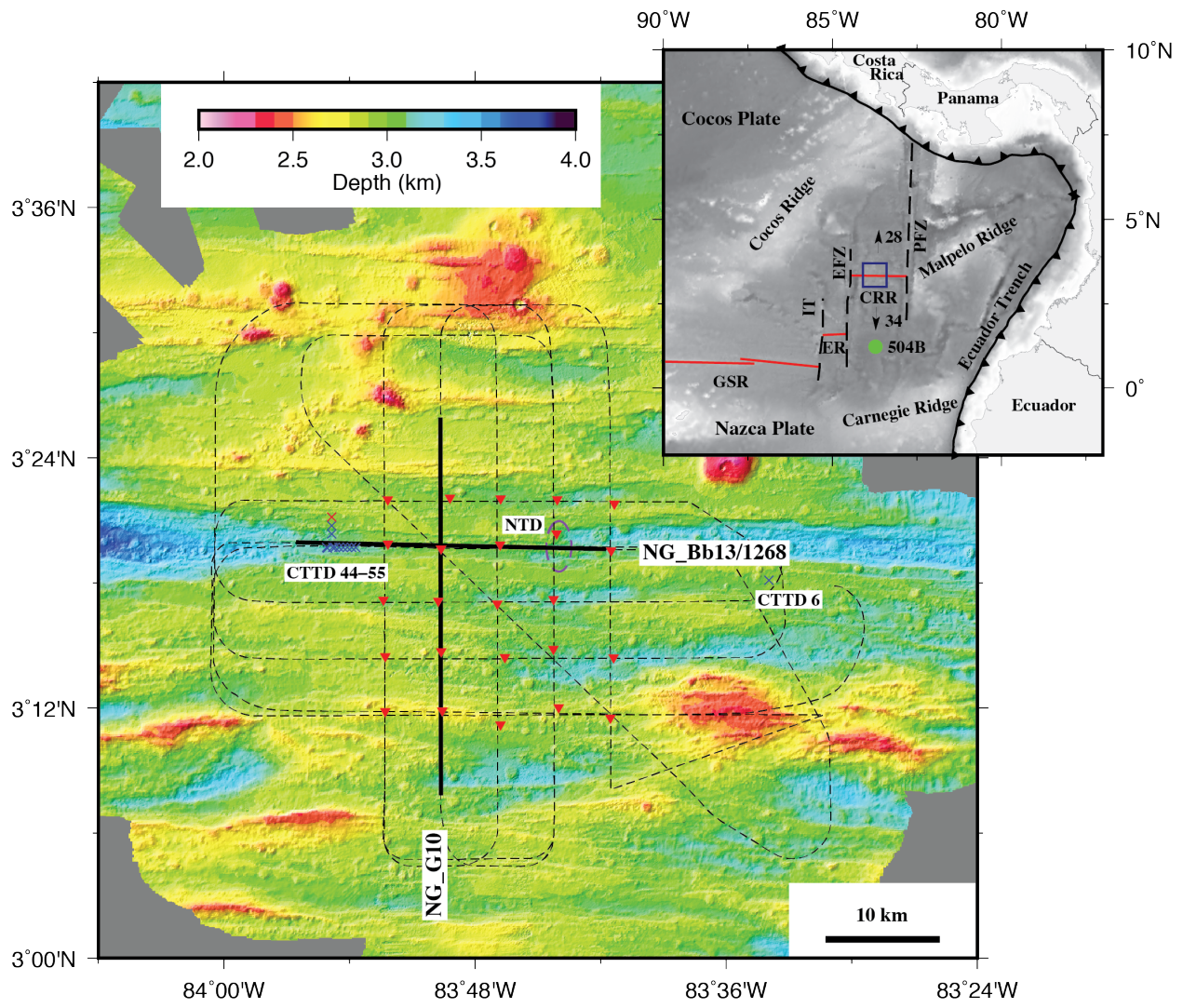
656

Symbol	Meaning	Value/Units
A_d	Area of discharge zone	m^2
A_m	Area of AML	m^2
c_p	Specific heat of seawater	$4\text{-}5 \times 10^3 \text{ J kg}^{-1} \text{ }^\circ\text{C}^{-1}$
c_m	Specific heat of magma	$1.1 \times 10^3 \text{ J kg}^{-1} \text{ }^\circ\text{C}^{-1}$
F_0	Buoyancy flux	$m^4 \text{ s}^{-3}$
g	Acceleration due to gravity	9.8 m s^{-2}
H	Hydrothermal heat output	Watts
H_m	AML heat content	J
k	Permeability	m^2
L	Latent heat of magma	$4 \times 10^5 \text{ J kg}^{-1}$
N^2	Brunt-Väisälä frequency	s^{-2}
Q	Volume flux of fluid	$m^3 \text{ s}^{-1}$
T_m	Magma liquidus temperature	1200°C
T_v	Hydrothermal vent temperature	350°C
V_m	Volume of melt	m^3
z	Vertical coordinate	
Z^*	Maximum plume rise height	m
<i>Greek symbols</i>		
α	Thermal expansion coefficient of seawater	$1.5 \times 10^{-4} \text{ }^\circ\text{C}^{-1}$
α_d	Thermal expansion coefficient of hydrothermal fluid in discharge zone	$10^{-3} \text{ }^\circ\text{C}^{-1}$
δ	Thermal boundary layer thickness	m
λ	Thermal conductivity of magma	$2.0 \text{ W m}^{-1} \text{ }^\circ\text{C}^{-1}$
ρ	Fluid density	kg m^{-3}
ρ_0	Background seawater density	1000 kg m^{-3}
ρ_m	Magma density	2700 kg m^{-3}
ν_d	Kinematic viscosity of hydrothermal fluid	$10^{-7} \text{ m}^2 \text{ s}^{-1}$

657

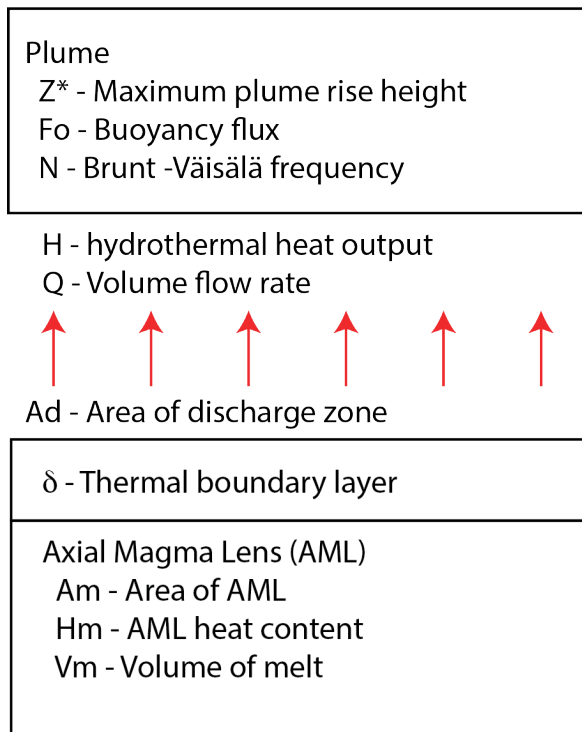
658

659



660
661

Figure 1.



662
663

Figure 2.

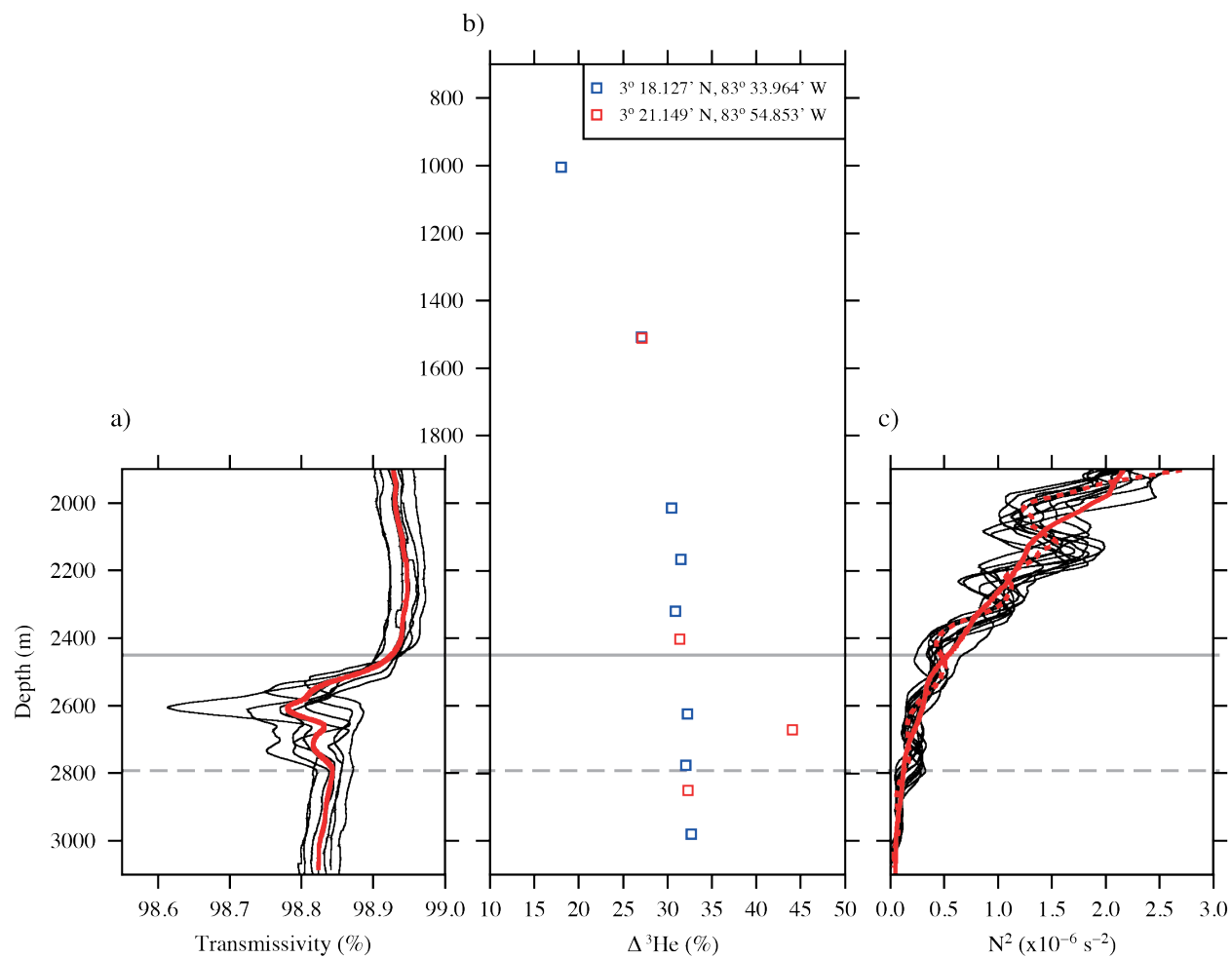
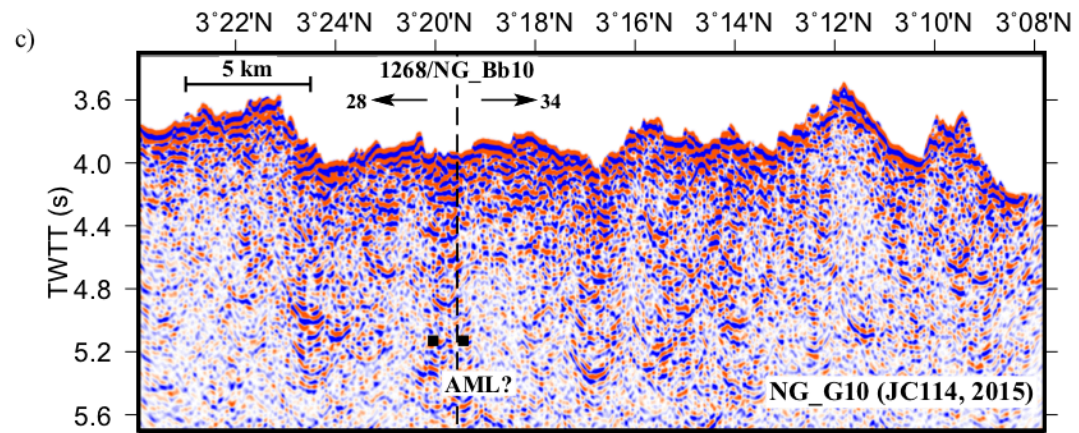
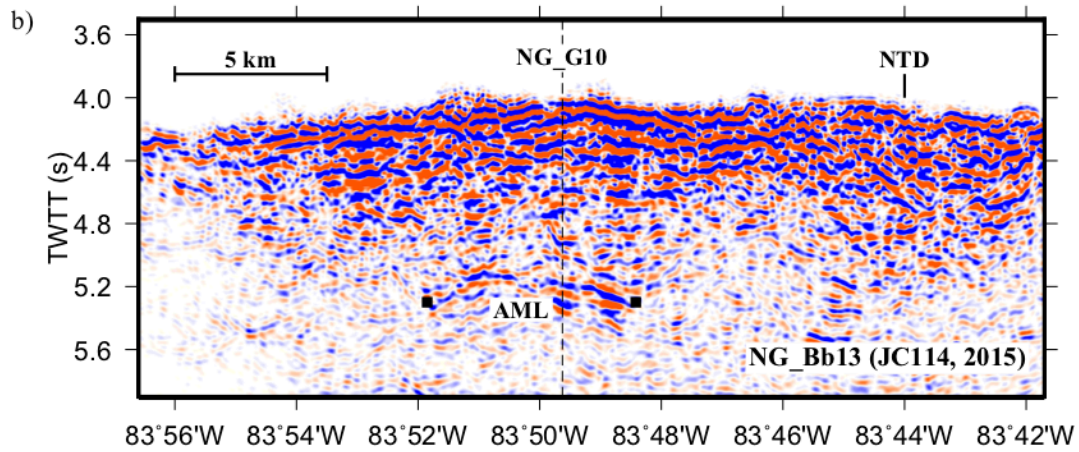
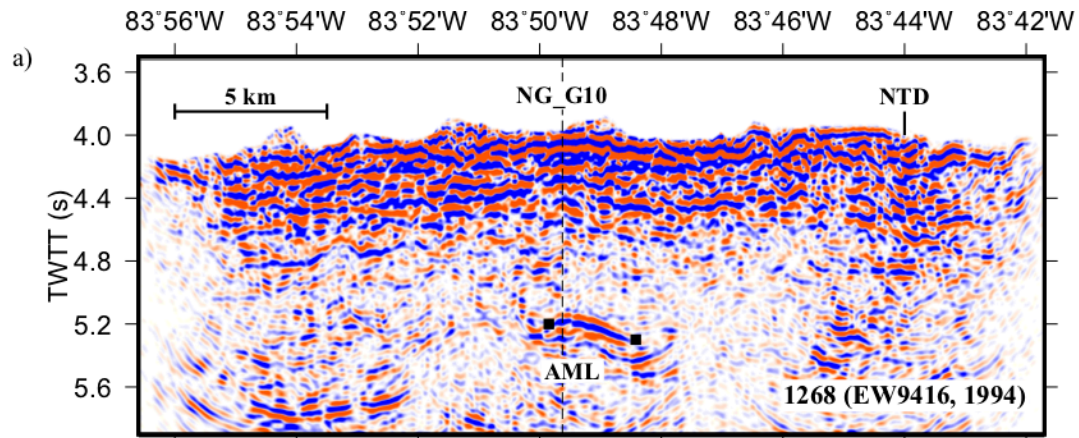


Figure 3.



665

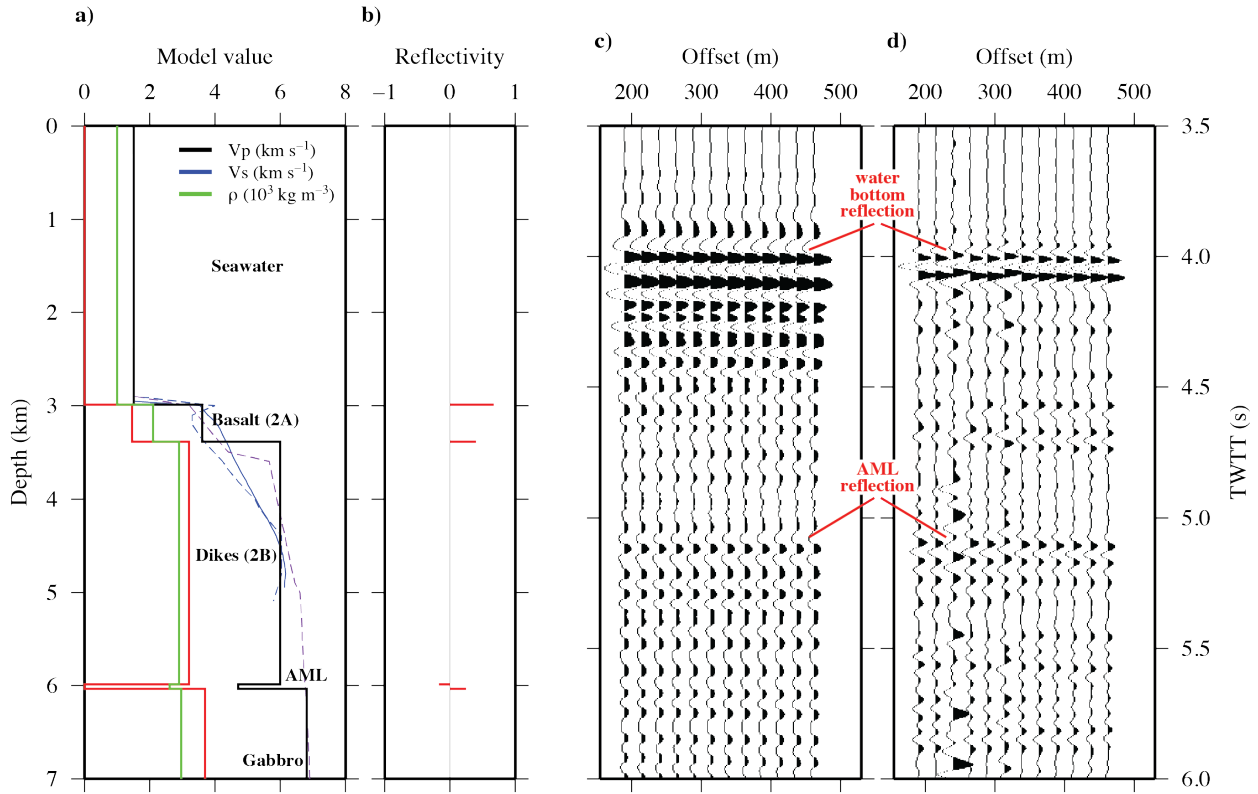
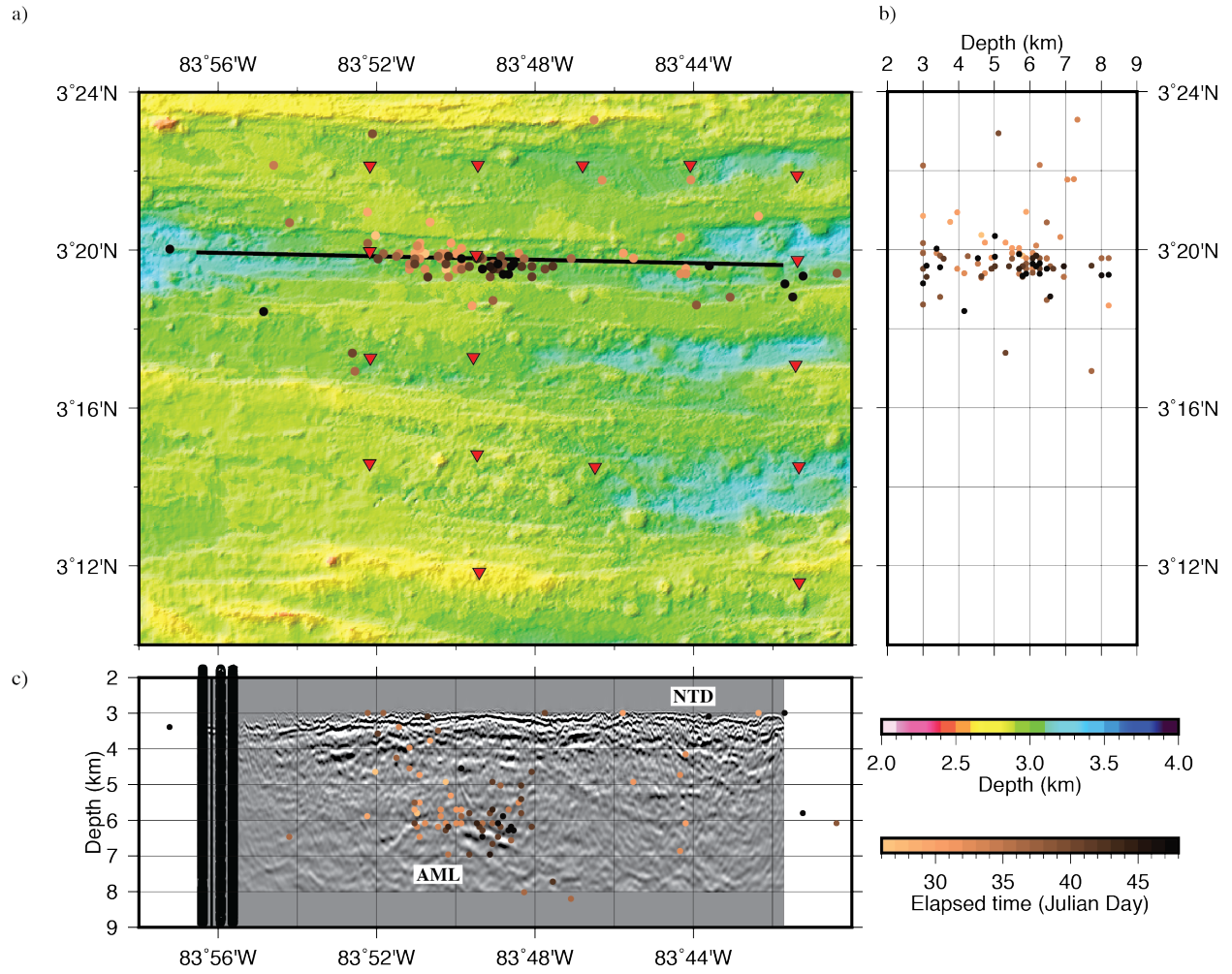


Figure 5.



667

Figure 6.